Stability Control for Wind in Weak Grids

Yin Li, *Student Member, IEEE*, Lingling Fan, *Senior Member, IEEE*, Zhixin Miao, *Senior Member, IEEE*

***Abstract*—4 Hz oscillations and 30 Hz oscillations have been observed in real world wind farms with weak grid interconnections. Such stability issues limit wind power delivery. This paper proposes mechanism-based feedback control strategies suitable for vector control-based voltage source converters (VSCs) employed in Type-3 and Type-4 wind to enhance the overall system stability. Using a simplified linear model, we first demonstrate that the root cause of weak grid stability issue is due to the coupling of power delivery and voltage at the point of common coupling (PCC). Increasing power delivery leads to a reduction in the PCC voltage. This relationship establishes a mechanism that may lead to instability in weak grid scenarios. The proposed control strategies reduce the coupling between power and voltage. Two feedback control strategies are introduced to modulate the power order or dc-link voltage order with either the d-axis current or the PCC voltage as the input signal. The control strategies are tested on analytical models and MATLAB/SimPowerSystems testbeds of Type-3 wind and Type-4 wind. The PCC voltage feedback control demonstrates excellent capability of stability enhancement. With the proposed control, power delivery of wind can be significantly improved.**

***Index Terms*—Feedback control; stability; wind; weak grid.**

I. Introduction

Stability issues due to wind in weak grids have been investigated in the literature, e.g., [1]–[3]. In real-world operation of wind farms in weak grids, Texas sees 4 Hz oscillations [4] and the west China region sees 30 Hz oscillations [5]. In our prior work [6]–[8], analysis has been conducted to identify the mechanism of instability and critical influencing factors. In summary, the following knowledge has been gained from [6]–[8].

1) Due to vector control employed in VSCs, increasing active power will lead to a reduction in the PCC voltage. This mechanism introduces a potential unstable feedback loop [6].
2) When the converter is in power control mode, phase-locked-loop (PLL) with higher bandwidth is better for stability [7].
3) When the converter is in power control mode, low-frequency oscillations are dominant. When the converter is in dc-link voltage control mode, both low-frequency oscillation mode and subsynchronous oscillation (SSO) mode exist. PLL plays a role in determining which mode is dominant [8].
4) Compared to the dc-link voltage control model, a VSC in power control mode can operate in a much weaker grid [8]. In other words, power control mode has advantages over dc-link voltage control mode in weak grid operation.

Yin Li, Lingling Fan, and Zhixin Miao are with the Department of Electrical Engineering, University of South Florida, Tampa, FL 33420 USA e-mail: linglingfan@usf.edu.

The objective of this paper is to further explore converter control strategies to enhance stability. In the literature or industry practice, there are four categories of strategies to improve stability for VSC operation in weak grids. In the first category, devices are used in the grid to improve stability margin. For example, studies for ERCOT show that using shunt reactive power compensation can enhance wind weak grid operation [9].

The second category deals with converter control structures. Type-4 wind's grid-side converter (GSC) is either in dc-link voltage control mode or active power control mode [10] (Chapter 9). According to [11], small size Type-4 wind employs dc-link voltage control for GSC while large-size wind prefers to have GSC behave more like a voltage source. A grid dynamic study from Siemens [12] indicates that large size Type-4 wind's GSCs are usually in power control mode. This fact aligns with our finding that a VSC with power control mode has advantages over dc-link voltage control mode for weak grid operation.

In the third category, vector control and PLL are abandoned. Instead, converter control is designed to emulate a synchronous generators [13], [14].

In the fourth category, vector control is modified or enhanced for weak grid operation, e.g., [15], [16]. [15] aims to compensate the angle error between the PCC voltage and the PLL output. [15] found that the deviations of the converter current in dq frame, Δi_d and Δi_q, are linear with angle error and PCC voltage ($\Delta V_{\rm PCC}$) respectively. This finding aligns with the finding shown in our prior work [7] (Eq. (14) and (15)). Two compensation modules are used. The first one uses Δi_d as input and its output modulates the PLL angle. The second one uses Δi_q as input and its output modulates the converter voltage magnitude order. The modified vector control can operate at short circuit ratio (SCR)at 1 when power reaches 60% of nominal level. In [16], the authors found that with only inner control, a VSC in a very weak grid (SCR =1) is always stable. After the outer control loops (power control and ac voltage control) are added, instability appears due to nonlinearity. Hence, the authors added decoupling effect in the outer loop to overcome nonlinearity. The added control employs gain scheduling technique. Under different operation conditions, gains should be calculated respectively. When SCR =1, the proposed control can achieve maximum power output at 89% of the nominal level.

Our approach falls into Category 4. We aim to enhance stability through vector control-based VSC.

Our Contributions: The proposed feedback control strategies are based on a thorough understanding of the mechanism of wind in weak grid stability. Compared to the design in [15], [16], the control strategy is simple and easy to implement. They are suitable for systems of different parameters

and varying operating conditions. What is more, the power transfer capacity of VSC in weak grid operation is significantly improved. Our study results demonstrate a better weak grid operating capability compared to those in [16] and [15]. For VSCs in power control mode, close to steady-state limit power delivery can be achieved. For VSCs in dc-link voltage control mode, 0.97 pu power can be delivered.

In this research, validation of control is conducted using not only two analytical models but also two wind farm testbeds (Type-3 and Type-4) in MATLAB/SimPowerSystems. The two testbeds are based on average models and include the full details of practical wind farms. The validation of this paper verifies the practicality of the proposed stability control.

Organization: The rest of the paper is organized as follows. In Section II, the mechanism of instability is analyzed based on a simple linear model. Principles of the stability enhancement strategies are presented. In Section III, the feedback control is implemented in the two analytical models and the eigenvalue loci are used to analyze its performance. In Section IV, the feedback control strategies are implemented in SimPowerSystems testbeds. Section V concludes the paper.

II. Principles of Stability Enhancement

A. Recap of [6]

In [6], a simple model is derived to explain instability issues for wind in weak grids.

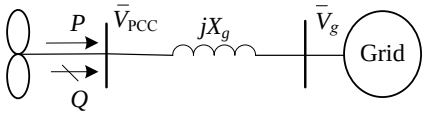

Fig. 1: A wind farm grid integration system.

Fig. 1 presents a wind farm connected to a grid through a transmission line represented by a reactance X_g. A wind farm of Type-3 or Type-4 is assumed as a controllable current source. This assumption is also adopted in GE's generic wind farm models [17]. Type-3 wind has an additional shunt admittance to represent double-fed induction generator's circuit components.

Converter's vector control is based on the PCC voltage, i.e., the dq-frame's d-axis is aligned with the PCC voltage space vector. Hence $P = V_{\rm PCC} i_d$ and $Q = -V_{\rm PCC} i_q$. For a given PCC voltage, adjusting the d-axis current will adjust the active power P but not influence the reactive power Q at steady-state. Similarly, adjusting the q-axis current will adjust the reactive power Q but not influence P. Converter's outer control loops generate dq-axis current orders and a first order delay represents the current control effect.

The relationship between the wind farm currents, PCC voltage, and the grid voltage is as follows.

$$v_{{\rm PCC},d} + j v_{{\rm PCC},q} = jX_g(i_d + j i_q) + \overline{V}_g \tag{1}$$

It is assumed that $\overline{V}_{\rm PCC}$ is aligned with the d-axis so (1) can be rewritten as the following:

$$\begin{aligned} V_{\rm PCC} = v_{{\rm PCC},d} &= -X_g i_q + V_g \cos\delta \\ 0 = v_{{\rm PCC},q} &= X_g i_d - V_g \sin\delta \end{aligned} \tag{2}$$

where δ is the angle by which $\overline{V}_{\rm PCC}$ is leading $\overline{V}_g$. Its range is $\left[-\frac{\pi}{2}, \frac{\pi}{2}\right]$. Combining two equations in (2) leads to the following:

$$V_{\rm PCC} = -X_g i_q + \sqrt{V_g^2 - (X_g i_d)^2} \tag{3}$$

$$\Rightarrow \Delta V_{\rm PCC} = -X_g \Delta i_q - c \Delta i_d \tag{4}$$

where $c = X_g / \sqrt{\left(\frac{V_g}{X_g i_d}\right)^2 - 1}$. $c > 0$ and $c \to \infty$ if i_d is close to the short circuit current V_g / X_g.

Eq. (4) indicates that an increase in the d-axis current leads to a reduction in the PCC voltage. Further, the linear expression of P versus $V_{\rm PCC}$ and i_d can be found as follows.

$$P = V_{\rm PCC} i_d \Rightarrow \Delta P = i_d \Delta V_{\rm PCC} + V_{\rm PCC} \Delta i_d \tag{5}$$

The entire system's linear model including the circuit and vector control is now obtained and shown in Fig. 2.

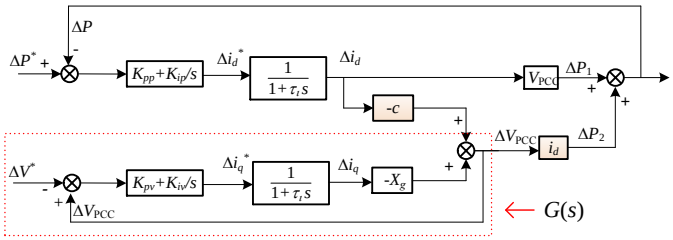

Fig. 2: Linear system block diagram in [6].

In [6], the power control loop is opened and an open-loop transfer function is derived from the power order to the power measurement and shown in (6).

$$\text{Loop}_1 = \frac{K_{ip}(\tau_p s + 1)}{s} \frac{1}{1 + \tau_i s} (V_{\rm PCC} - c i_d G) \tag{6}$$

where $\tau_p = K_{pp}/K_{ip}$.

It is found that under high power transfer and weak grid conditions, the open-loop transfer function will have a zero at the real-axis of the right half plane (RHP), which may lead to poorly damped or undamped oscillations.

B. Mechanism of Instability

The explanation offered in [6] adopts control system terminology: a RHP zero in the open-loop system. In this subsection, the instability mechanism will be examined from the converter control design perspective.

A numerical example is first presented to demonstrate that an increment in the d-axis current (i_d) leads to a decrement in the PCC voltage ($V_{\rm PCC}$). Note that if the dq-axis is aligned with the grid voltage, an increment in the d-axis current should lead to an increment in the PCC voltage. Thus, it is indeed the PCC voltage based vector control that introduces the counter-intuitive phenomenon.

Numerical example: Assume that the current control is in place and the dq-axis currents follow the current orders at steady-state. The q-axis current i_q will keep intact while the d-axis current i_d will have a 10% increase. Fig. 3 presents the phasor diagrams of the grid voltage, dq-axis currents, and the PCC voltage for the base case and the comparison case. The

grid reactance X_g is assumed to be 0.866 pu, the grid voltage V_g is 1 pu, and the PCC voltage is at 1 pu at the base case. Also at the base case, 1 pu real power is sent from the wind to the grid. This indicates that the PCC voltage phase angle is 60° ahead of the grid voltage angle. The d-axis is aligned with the PCC voltage phasor and the d-axis current i_d is 1 pu. We can further find the q-axis current as -0.5774. The corresponding dq-axis current phasor are notated as $\overline{I}_d$ and $\overline{I}_q$ in Fig. 3.

In the comparison case (notated as superscript (1) in Fig. 3), there is 10% increase in i_d. Based on the KVL relationship presented in (2), it can be found that the angle of the PCC voltage phasor will increase to $\sin^{-1}\left(\frac{X_g i_d}{V_g}\right) = 72.3°$. i_q will be kept the same. However, the phase angle of $\overline{I}_q$ varies. The PCC voltage is shown to have a 20% decrease in its magnitude. The ratio of $\frac{\Delta V_{\rm PCC}}{\Delta i_d}$ is 2.

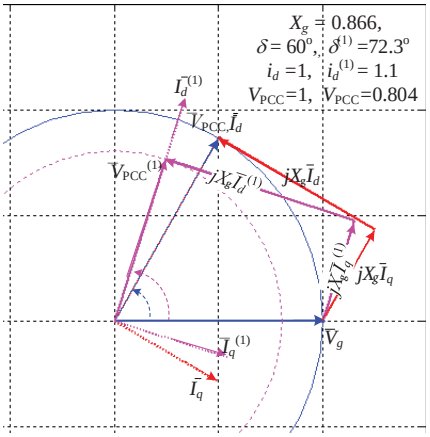

Fig. 3: An 10% increase in i_d leads to a 20% decrease in $V_{\rm PCC}$.

The example in Fig. 3 demonstrates that due to vector control, an increase in the power order will translate to an increase in the d-axis current order and further to a decrease in the PCC voltage if the q-axis current order keeps intact, or no voltage/var control is in place. Such effect should not be ignored as the ratio of $\frac{\Delta V_{\rm PCC}}{\Delta i_d}$ reaches 2 when SCR is 1.15 and more for a smaller SCR.

Note that if the grid is very strong and the impact of Δi_d to $\Delta V_{\rm PCC}$ can be ignored ($c = 0$), then the system is always stable. In power electronics converter design, a stiff PCC voltage is usually assumed (see Chapter 8 of [18]). Thus, in converter control design stage, weak grid instability issues cannot not captured. Stability issues appear once vector control-based VSCs are interconnected to weak grids.

Effect of voltage and power control: Examine a case without voltage control when $G(s) = 1$. The highlighted path from Δi_d to $\Delta V_{\rm PCC}$ and further to ΔP_2 in Fig. 2 introduces a destabilizing mechanism. If $ci_d > V_{\rm PCC}$, then the system is unstable. With voltage control, the block $G(s)$ can be found as

$$G(s) = \frac{s(1+\tau_i s)}{\tau_i s^2 + (1 + X_g K_{pv})s + X_g K_{iv}}. \quad (7)$$

At steady-state, $G(s \to 0) = 0$. If the bandwidth of $G(s)$ is very high, then in the lower frequency range, $G(s)$ can be viewed as 0. Thus, faster voltage control will be beneficial for stability.This point will be further confirmed by the root loci plots. The root loci for Loop$_1$ are plotted and shown in Fig. 4. The parameters are: $X_g = 1$ or SCR$= 1$, $i_d = 0.9$, $\tau_i = 0.05$, and $(K_{pp}, K_{ip}) = (0.25, 25)$.

Two sets of voltage controller parameters are compared.

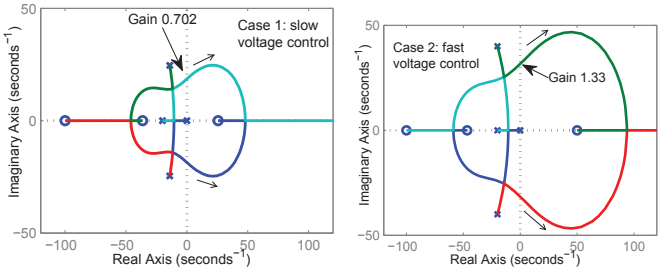

Fig. 4: Root loci for two sets of voltage control parameters. Left: Case 1: slower voltage control, $(K_{pv}, K_{iv}) = (0.4, 40)$. Right: Case 2: faster voltage control, $(K_{pv}, K_{iv}) = (1, 100)$

Root loci plots show that the system has four loci representing by four different colors. Two loci move to the RHP when the gain changes from 0 to ∞ since there is a zero in the RHP. Note that the gain is 1 when the loop is closed. Case 1 is unstable since the marginal gain is 0.702. When the gain is 1, there will be two closed-loop poles located in the RHP. On the other hand, Case 2 is stable indicated by the marginal gain being 1.33.

Remarks:

1) Faster voltage control is better for weak grid stability.
2) From the loci movement trends shown in Fig 4 and Loop$_1$ expression in (6), it can be found that if τ_p is kept constant, then a smaller gain of the power control K_{ip} makes the closed-loop system more stable. Thus, slower power control is better for weak grid stability.

C. Stability Enhancement Strategies

The linear block diagram in Fig. 2 can be aggregated in different ways. Fig. 5 shows two linear diagrams.

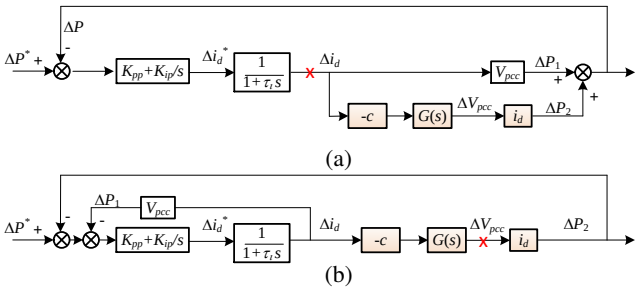

Fig. 5: Linear block diagrams. (5a): Sys 1. (5b): Sys 2.

The open-loop systems are obtained by breaking the points marked by the red crosses. Sys 1's open-loop gain is the same as Loop$_1$. Root loci for the two loop gains are plotted in Fig. 6. For both systems, there are two root loci moving to the RHP, which indicates potential instability.

Based on the two diagrams, two feedback control strategies are proposed to suppress the effect of $\Delta V_{\rm PCC}$ on real power

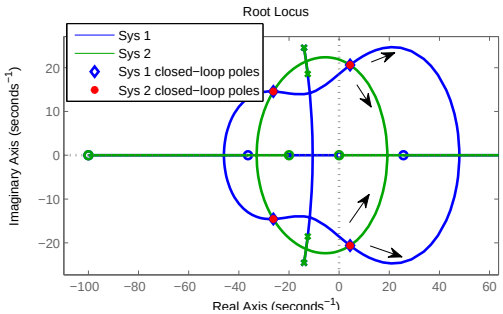

Fig. 6: Root loci for two models in Fig. 5.The system parameters are: $X_g = 1$, $i_d = 0.9$, $\tau_i = 0.05$, $(K_{pp}, K_{ip}) = (0.25, 25)$, and $(K_{pv}, K_{iv}) = (0.4, 40)$.

ΔP, shown in Fig. 7. The first strategy is to modulate the power order using the d-axis current feedback. The effect is same as increasing the gain from Δi_d to ΔP_1. The dotted loop shown in Fig. 7a presents the intended effect. In control implementation, this is equivalent to introduce a negative feedback loop with Δi_d as the input signal to modulate the power order. The solid blue line presents the control implementation.

The second strategy is to modulate the power order using the PCC voltage $\Delta V_{\rm PCC}$ as shown in Fig. 7b. The effect is same as decreasing the gain from $\Delta V_{\rm PCC}$ to ΔP_2. The dotted loop shown in Fig. 7b presents the intended effect. In control implementation, this is equivalent to introduce a positive feedback loop with $\Delta V_{\rm PCC}$ as input signal to modulate the power order.

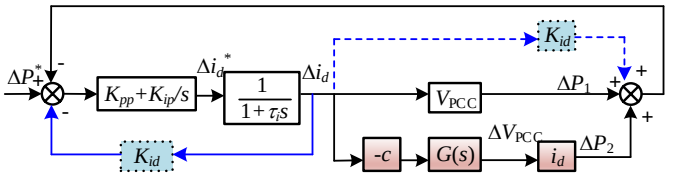

Fig. 7: Linear block diagram with feedback controls. (a): Δi_d as input signal. (b): $\Delta V_{\rm PCC}$ as input signal.

Analysis of the control strategy: The current feedback control cannot achieve a complete power/voltage decoupling. On the other hand, the voltage feedback control can indeed achieve a complete decoupling if the gain K_v is chosen to be the same as i_d. Consider the worst scenario of full power exporting, the gain of the voltage control can be chosen to be the rated current (e.g., 1 pu) to achieve power/voltage decoupling. The control is simple and easy to implement.

III. Analytical Model-Based Analysis

The simplified model used for mechanism analysis and stability control design ignores PLL dynamics, current feedback control, converter filter, transmission line resistance, and grid dynamic. Our prior work [7] indicates that ignoring PLL dynamics leads to optimistic evaluation of stability. Hence, to investigate the stability control's performance, the feedback controls are implemented in the analytical models of Type-4 wind systems considering GSC control, current control, converter filter, transmission line resistance, and grid dynamics. The topology of the system is shown in Fig. 8. Two analytical models will be used for evaluation. Model 1 is developed in [7] with GSC in active power control mode. Model 2 is developed in [8] with GSC in dc-link voltage control mode. Model 2 also includes the dc-link capacitor dynamics.

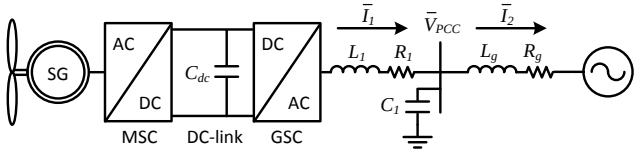

Fig. 8: Topology for the analytical model.

Initialization procedure: Take Model 2 (shown in Fig. 9b) as an example. The initialization procedure will assign values for all state variables as well as $P_{\rm wind}$. Model 2 has 13 state variables excluding the state variables related to the stability control. The state variables include one state variable related to dc-link capacitor ($V_{\rm DC}^2$), two state variables related to the PI controllers in the outer loop (x_1 and x_2), two state variables related to the PI controllers in the inner loop (x_3 and x_4), six state variables related to the grid dynamics (the PCC voltage, the converter current, and the line current, all in the grid frame), and two state variables related to second-order PLL (one being the frequency deviation $\Delta\omega$ and the other being the output angle $\Delta\theta$).

Initial values for a few state variables can be quickly found without any computation. The steady-state value for $V_{\rm DC}^2$ is 1 pu. The steady-state value for frequency deviation from PLL $\Delta\omega$ is 0. The rest needs to be calibrated.

Since the GSC is in real power and PCC voltage control mode, we may assume that the PCC voltage $V_{\rm PCC}$ is given. Real power flowing from PCC bus to the grid is also given. As a first step, we may examine a two-bus network with the PCC bus as a PV bus, the grid as a slack bus to solve a power flow problem and find the angle of the PCC bus. The steady-state value for $\Delta\omega$ is 0 and $\Delta\theta$ is the same as the PCC voltage phase angle $\Delta\theta_{\rm PCC}$. Consequently, the line current $\bar{I}_2$ and the converter current $\bar{I}_1$ can be found. Real and imaginary values of the currents correspond to the dq-axis currents in the grid frame: $\bar{I}_2 = i_{2d}^g + ji_{2q}^g$ and $\bar{I}_1 = i_{1d}^g + ji_{1q}^g$. With the PCC voltage phasor and converter current phasor information, we may find the steady-state converter voltage phasor $\bar{V}$ and its dq-components (v_d^g, and v_q^g).

The converter current and voltage in the grid frame can be converted into converter-frame based.

$$i_{1d}^c + ji_{1q}^c = (i_{1d}^g + ji_{1q}^g)e^{-j\Delta\theta_{\rm PCC}}$$
$$v_d^c + jv_q^c = (v_d^g + jv_q^g)e^{-j\Delta\theta_{\rm PCC}}$$

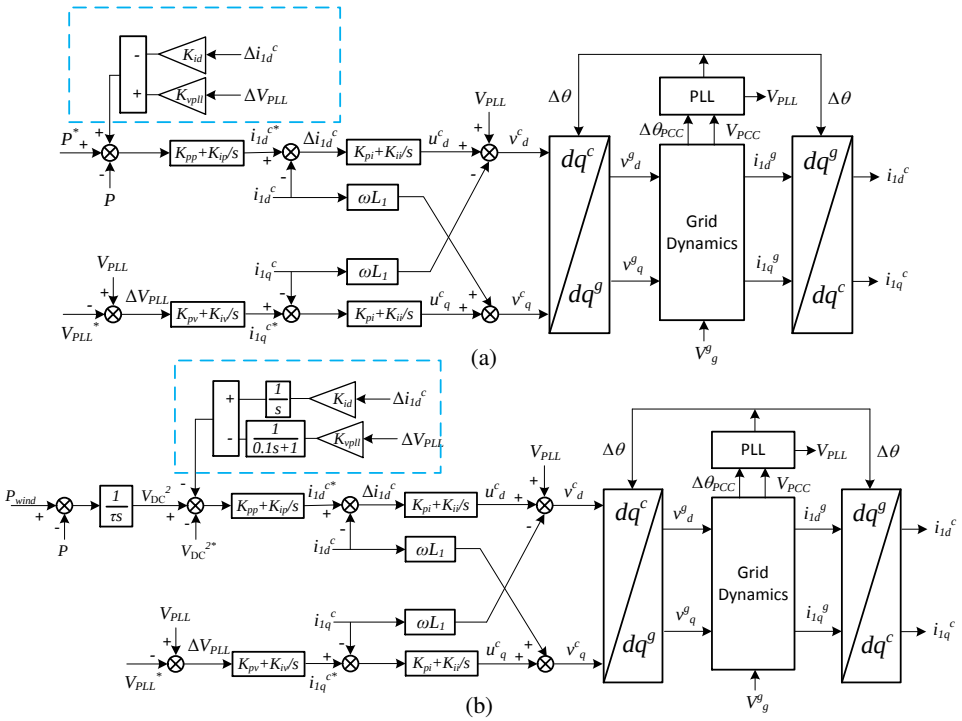

Fig. 9: Control implementation in Model 1 (9a) and Model 2 (9b). Superscripts g and c notate grid and converter reference frames respectively.

P_{wind} at steady-state equals the real power delivered from the converter: $P_{\text{wind}} = v_d^c i_{1d}^c + v_q^c i_{1q}^c$.

The initial states related to the outer loops can be found as $x_1 = i_{1d}^c$, $x_2 = i_{1q}^c$. The initial states related to the inner loops can be found as $x_3 = v_d^c + \omega L_1 i_{1q}^c - V_{\text{PCC}}$, $x_4 = v_q^c - \omega L_1 i_{1d}^c$. Thus, all state variables will have their steady-state values assigned.

A. Model 1: Power Control Mode

Fig. 9a shows the analytical model with GSC in active power and ac voltage control mode. Either the PCC voltage deviation measured by PLL (ΔV_{pll}) or the converter d-axis current deviation (Δi_{1d}) will be used to modulate the real power order. Proportional control is used.The grid dynamics block uses the grid reference frame with its d-axis aligned with the grid voltage while the converter control blocks use the converter reference frame with its d-axis aligned with the PCC voltage.

The performance of the feedback control can be analyzed based on the eigenvalue loci generated from the analytical model. The parameters used in the analytical model are listed in Table I in Appendix.

The system is assumed to operate at 0.9 pu power and the PCC voltage is at 1 pu. Eigenvalue loci are plotted in Fig. 10 to show the effect of feedback gains in power and ac voltage (PV) control. For PV control, the marginal stable condition is $X_g = 0.86$ pu. Fig. 10a and Fig. 10b show the effect of K_{id} or K_{vpll} on system eigenvalues when $X_g = 0.88$ pu. Fig. 10b indicates that the best value for the gain K_{vpll} is at 0.8 or 0.9. Indeed, this finding corroborates the observation based on the simplified model: when the gain matches i_d (in this case, $i_d = 0.9$), a complete power/voltage decoupling is achieved.

Fig. 10c and Fig. 10d show the eigenvalue loci with X_g increasing when control gain K_{id} or K_{vpll} is fixed at 10 or 0.9, respectively.

In control design, small gain is preferred to avoid hitting limits. It can be found that the current-based stability control requires a much larger gain. Hence, the voltage-based stability control is preferred over the current-based stability control. Fig. 10d demonstrates that with the voltage-based stability controller ($K_{vpll} = 0.9$), the system is stable even when X_g increases to 1.1 pu. Note that the steady-state power transfer limit for a transmission line is approximately $1/X_g$ if voltages at both ends are 1 pu. When $X_g = 1.1$, the power limit is 0.91. With the stability control, a VSC can achieve a power transfer level close to the steady-state limit.

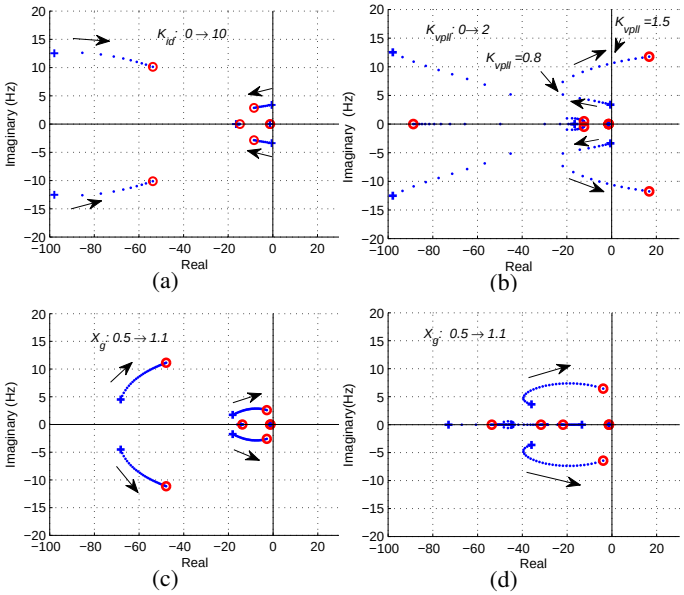

Fig. 10: Eigenvalue loci for the power control. $P = 0.9$, $V_{\text{PCC}} = 1$. (10a): increase K_{id} from 0 to 10 with $X_g = 0.88$ pu. (10b) increase K_{vpll} from 0 to 2 with $X_g = 0.88$ pu. (10c): increase X_g with $K_{id} = 10$. (12d) increase X_g with $K_{vpll} = 0.9$.

B. Model 2: DC-link Voltage Control Mode

When the GSC is in dc-link voltage control mode, the dc-link capacitor dynamics should be modeled. Analytical model built in [8] will be used to test the performance of the stability controller.

In this case, the stability control should be implemented to modulate the dc-link voltage reference instead of the power order. To have a similar effect of modulating the power order, an integrator is used. Dc-link voltage should be kept at certain level. Experiments show that modulating the dc-link voltage reference with the output from an integrator control with PCC voltage input may lead to increase or reduction of the dc-link voltage at steady-state. Therefore, a high pass filter (HPF) ($\frac{s}{0.1s+1}$) is used after the integrator to filter out the dc component. Combining the integrator $1/s$ and the HPF leads to a low pass filter (LPF) ($\frac{1}{0.1s+1}$). The control implementation is presented in Fig. 9b.

Fig. 11 compares the different dynamic responses of the system: without voltage-based stability control, with an integrator-based voltage feedback control, and with an additional HPF. The responses are the output power, dc-link voltage, ΔV_{pll}, and the output of the stability control or compensation on $V_{\rm DC}$. It indicates although the integrator-based feedback control of ΔV_{pll} can improve the stability, a dc component is added to the dc-link voltage order at steady-state. With the HPF, the dc component is eliminated.

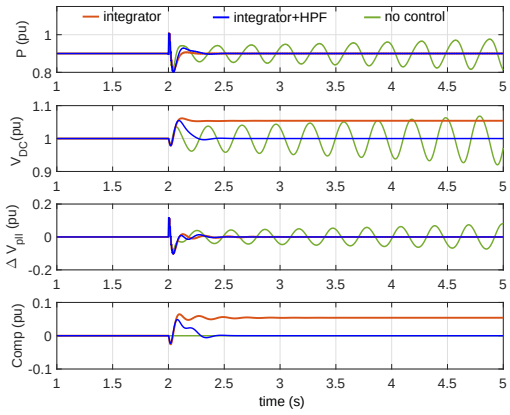

Fig. 11: Comparison of dynamic responses with and without the HPF. $X_g: 0.5 \rightarrow 0.61$.

The eigenvalue loci for the system of Fig. 9b are plotted in Fig. 12 assuming 0.90 power. The marginal stable condition is $X_g = 0.6$ pu. The upper two plots Fig. 12a and Fig. 12b demonstrate that effect of gain of the stability controller K_{id} or K_{vpll} when $X_g = 0.61$ pu. 4000 is chosen for K_{id} and 2 is chosen for K_{vpll}. The lower two plots present the closed-loop system eigenvalues for a varying X_g with fixed controller gain ($K_{id} = 4000$, or $K_{vpll} = 2$).

It can be seen that the control can enhance system stability. For VSC in dc-link voltage control mode, the gain required for the current-based stability control is very large.Fig. 12d demonstrates that the marginal stable condition can be increased to $X_g = 1.02$ pu with the voltage-based stability control installed.

Fig. 13 presents the time-domain responses with a small disturbance (0.01 pu reduction in the ac voltage order) at $t = 2$

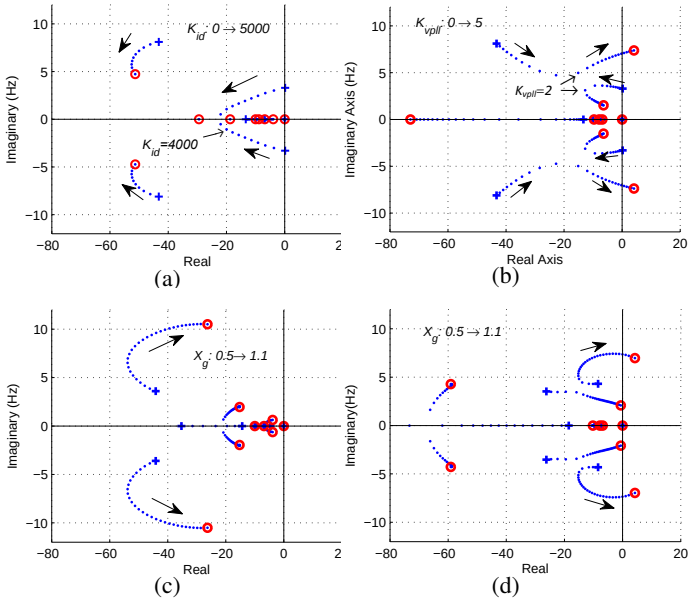

Fig. 12: Eigenvalue loci for the dc-link control. (12a): increase K_{id} from 0 to 5000 with $X_g = 0.61$ pu. (10b) increase K_{vpll} from 0 to 5 with $X_g = 0.61$ pu. (10c): increase X_g with $K_{id} = 4000$. (12d) increase X_g with $K_{vpll} = 2$.

s. The grid reactance X_g is 1 pu. With the PCC voltage-based stability control, the wind farm can transfer more than 0.9 pu power to a very weak grid (SCR $= 0.995$). It can be seen when $P = 0.97$, the system has two oscillation frequencies, one at 7 Hz and the other at 2 Hz. The time-domain simulation results corroborate with the eigenvalue analysis in Fig. 12d where two modes, one at 7 Hz and the other at 2 Hz, move towards the RHP when the grid becomes weaker.

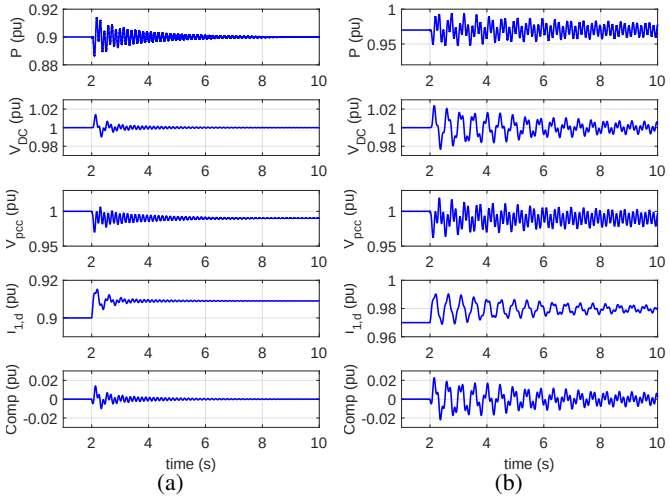

Fig. 13: Time-domain simulation results with $K_{vpll} = 2$: (13a): $X_g = 1.0$ pu, $P = 0.9$ pu; (13b): $X_g = 1.0$ pu and $P = 0.97$ pu.

IV. Validation in MATLAB/SimPowerSystems

The final stage validation is carried out in two testbeds in MATLAB/SimpPowerSystems. The testbeds aligns more with the real-world system with full dynamics and converter limitations modeled. The two testbeds are developed based on the demo testbeds of Type-3 wind and Type-4 wind in

SimPowerSystems. Topologies of Type-3 and Type-4 testbeds are shown in Fig. 14a and Fig. 14b. Type-3's rotor-side converter (RSC) is operated in power control mode. Since majority of power is delivered through RSC, we can view the Type-3 wind testbed similar to Model 1. Type 4's GSC is operated in dc-link voltage control mode. Hence we view the Type-4 wind testbed similar to Model 2.

Both wind farms are connected to the grid through 220 kV long transmission lines. The parameters of the two testbeds are listed in Table I and Table II in Appendix.

The testbeds impose limitations on converter currents. In the Type-3 wind testbed, the limitation of the RSC current is $\begin{bmatrix}0 & 0.9\end{bmatrix}$ pu. In the Type-4 wind testbed, the limitation is $\begin{bmatrix}-1.1 & 1.1\end{bmatrix}$ pu. Due to the converter current limitation, the testbeds cannot achieve the same operating limits identified by the analytical models. Nevertheless, testbeds can still demonstrate the effect of the proposed control. For the proposed control implementation, only one control signal is used at a time.

A. Type-3 wind

In Type-3 wind farm, the feedback control loop is implemented in RSC to modulate the power order. The wind farm power base is 100 MW while the rated power output of the wind farm is 90 MW or 0.9 pu. At steady-state, the rotating speed of the rotor is 1.25 pu and the slip is -0.25. With the total d-axis current from wind at 0.90 pu, the RSC d-axis current is 0.72 pu and the GSC d-axis current is 0.18 pu to the grid.

Fig. 15 presents wind output power P, dc-link voltage V_{DC}, PCC voltage V_{PCC}, RSC d-axis current order $i^*_{r,d}$, and the output from the stability control `Comp` for three scenarios: without control, with either voltage-based control ($K_{vpll} = 0.9$) or current-based control ($K_{id} = 10$). The gains are chosen based on the analysis in Section III. At $t = 2$ seconds, X_g changes from 0.5 pu to 0.88 pu to emulate a parallel line tripping event.

Without stability control, the system suffers 3 Hz oscillations. This performance aligns with the eigenvalue analysis presented in Fig. 10a or 10b. When the gain of the stability controller is 0, the system is at the marginal stability condition and the oscillation frequency is 3 Hz.

The current-based stability control does not improve the system stability. This is mainly due to i^*_{rd}, the d-axis RSC current order hitting converter limit. On the other hand, the voltage-based stability control makes the system stable.

We further test the system operating limit with voltage-based control equipped. Fig. 16 presents the dynamic responses when X_g changes from 0.5 pu to 1.0 pu and 1.01 pu, respectively. The system is stable when X_g changes from 0.5 to 1 and unstable when X_g changes from 0.5 to 1.01.

B. Type-4 wind

The power base of the Type-4 wind is 110 MW and the rated power is 100 MW or 0.9 pu. In Type-4 wind, the feedback control is implemented in GSC to modulate V_{DC} order. In the first case study, the system dynamic responses without

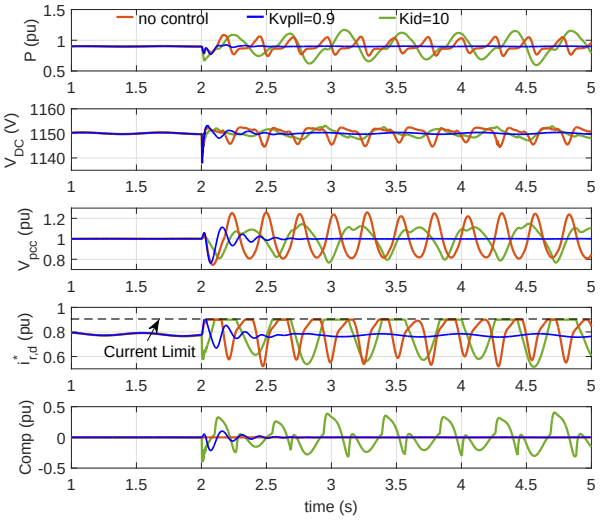

Fig. 15: Type-3 wind testbed simulation results: $X_g : 0.5 \rightarrow 0.88$ at 2 sec. Red line: no control; Blue line: voltage-based control ($K_{id} = 0$, $K_{vpll} = 0.9$); Green line: current-based control ($K_{id} = 10$, $K_{vpll} = 0$).

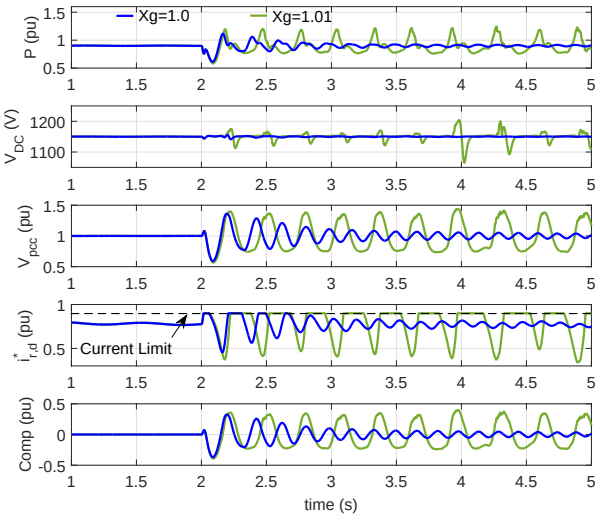

Fig. 16: Type-3 wind testbed results: with $K_{vpll} = 0.9, K_{id} = 0$, $X_g : 0.5 \rightarrow 1.0$ (blue line) and $X_g : 0.5 \rightarrow 1.01$ (green line).

control, with voltage or current-based control are compared. X_g was increased from 0.5 pu to 0.61 pu at 2 seconds to emulate an parallel transmission line tripping event. Fig. 17 presents the dynamic responses of P, V_{DC}, V_{PCC}, i^*_{1d} and stability controller output `Comp` for three scenarios: without control, with voltage-based or current-based control. The gains are chosen based on the analysis in Section III. Note that direction of the current is from the grid to the GSC as shown in Fig. 14b. Without stability control, 3 Hz oscillations appeared after the dynamic event. Both of voltage-based and current-based control make the system stable. The performance of the voltage-based control ($K_{vpll} = 2$) is better compared with the current-based control ($K_{id} = 4000$). Transients are shorter and overshoot is lower.

The system operating limits are examined with stability control equipped. The values of K_{id} and K_{vpll} are selected as 4000 and 2 respectively. Fig. 18 presents the dynamic

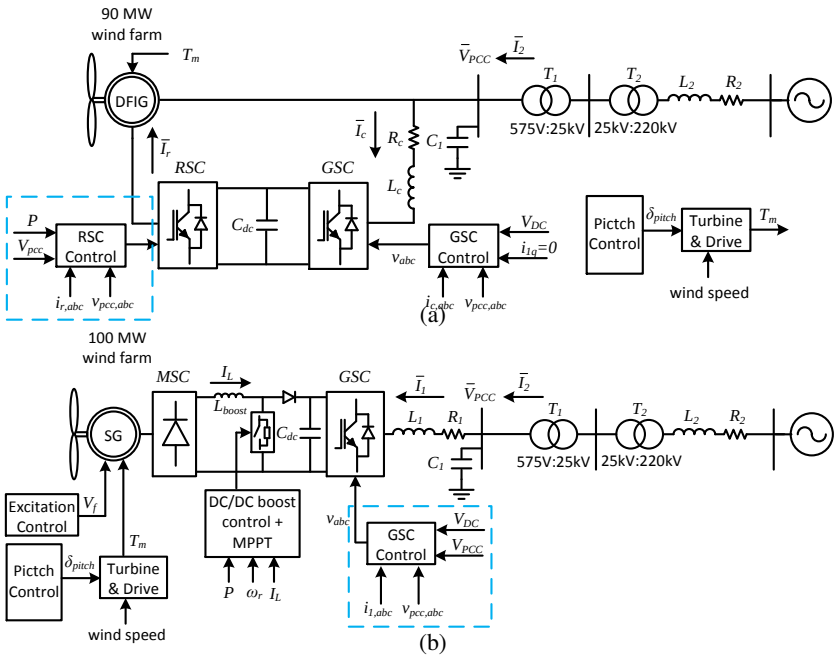

Fig. 14: MATLAB/SimPowerSystems Testbed: (14a): a 90 MW Type-3 wind farm is connected to a grid through a long transmission line. (14b): a 100 MW Type-4 wind farm is connected to a grid through a long transmission line.

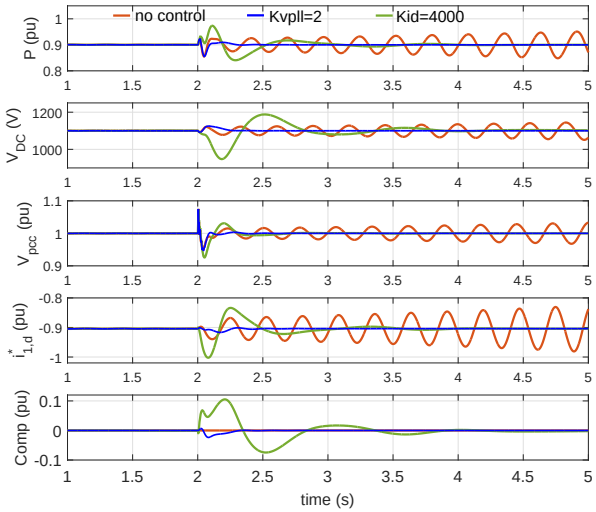

Fig. 17: Type-4 testbed results: $X_g : 0.5 \rightarrow 0.61$ at 2 sec. Red line: no control; Blue line: voltage-based control ($K_{id} = 0$, $K_{vpll} = 2$); Green line: current-based control ($K_{id} = 4000$, $K_{vpll} = 0$).

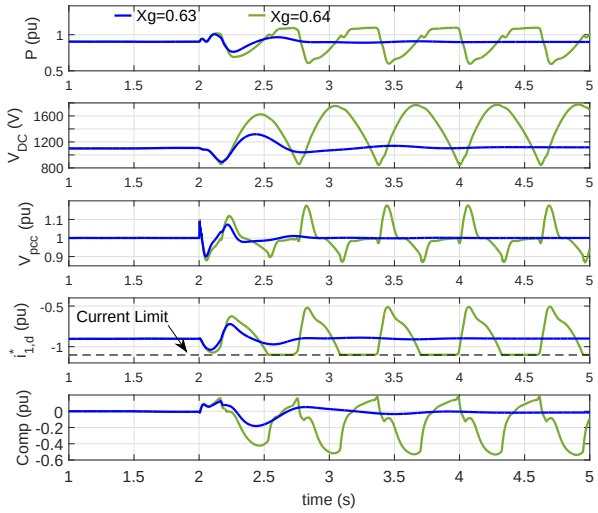

Fig. 18: Type-4 wind testbed results: with $K_{id} = 4000, K_{vpll} = 0$, $X_g : 0.5 \rightarrow 0.63$ (blue line), $X_g : 0.5 \rightarrow 0.64$ (green line).

responses of the system with current-based control for two large disturbances: $X_g : 0.5 \rightarrow 0.63$ and $X_g : 0.5 \rightarrow 0.64$. Because of the large overshoot, the current-based control ($K_{id} = 4000$) makes the converter current order hit the limits. The marginal stable condition changes from $X_g = 0.6$ pu to 0.63 pu.

Fig. 19 presents the dynamic responses of the system with voltage-based control ($K_{vpll} = 2$) for two large disturbances: $X_g : 0.5 \rightarrow 0.91$, $X_g : 0.5 \rightarrow 0.92$. It can be observed that the system is stable when X_g reaches 0.91 pu. The marginal stable condition is increased from $X_g = 0.60$ pu to 0.91 pu.

Remarks: Voltage-based stability control is preferred for both Type-3 and Type-4 wind. With this control, the system can operate in a much weaker grid. The limit of X_g increases from 0.88 pu to 1.0 pu for the Type-3 wind, and from 0.61 pu to 0.91 pu for the Type-4 wind.

V. Conclusion

Mechanism of stability issues related to wind in weak grids is thoroughly explained in this paper as the coupling between power and voltage. This coupling can be suppressed by introducing feedback control to modulate the power order or dc-link voltage order for vector control-based grid-side converters. Input signals can be either d-axis converter current or the PCC voltage. The feedback control is implemented in both analytical models and detail model-based MATLAB/SimPowerSystems Type-3 and Type-4 wind testbeds. The analytical models verify that the feedback control can improve weak grid operation for VSCs in both power control and dc-link voltage control modes. The MATLAB/SimPowerSystems testbeds demonstrate that the voltage-

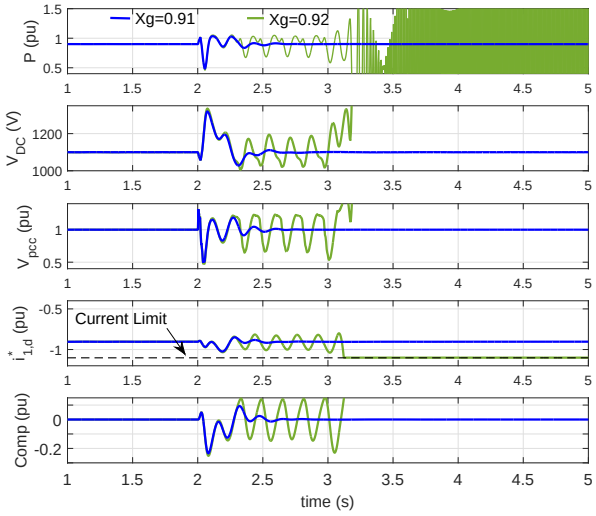

Fig. 19: Type-4 wind testbed results: with $K_{vpll} = 2, K_{id} = 0$, $X_g : 0.5 \rightarrow 0.63$ (blue line), $X_g : 0.5 \rightarrow 0.64$ (green line).

based control can significantly improve operation margins for both Type-3 and Type-4 wind.

APPENDIX

TABLE I: Parameters of Model 1 and Type-3 wind testbed

Parameter	Value (SI)	Per-unit (pu)
# of WT	60	
Rated power	1.5 MW	0.9
DC-link voltage	1150 V	
Rated voltage	575 V	1
Nominal freq.	60 Hz	1
$L_{ls}(X_{ls}), R_s$	94.5 μH, 5.6 mΩ	0.18, 0.023
$L'_{lr}(X'_{lr}), R'_r$	84.0 μH, 3.9 mΩ	0.16, 0.016
$L_m(X_m)$	1.5 mH	2.9
Inertial, poles	8.03 J, 6	
Friction factor	0.01	
C_{dc}	10 mF	
$L_c(X_c), R_c$	0.16 mH, 0.59 mΩ	0.3, 0.03
$C_1(B_1)$	2.9 mF	0.267
$L_{T1}(X_{T1}), R_{T1}$	0.165 mH, 6.25 mΩ	0.02, 0.002
$L_{T2}(X_{T2}), R_{T2}$	19.25 mH, 725 mΩ	0.03, 0.003
$L_2(X_2)$	$0.58 \rightarrow 1.35$ H	$0.45 \rightarrow 1.05$
R_2	$21.78 \rightarrow 50.82\ \Omega$	$0.045 \rightarrow 0.105$
Current control	$K_{pi} = 0.6,\ K_{ii} = 8$	
Power control	$K_{pp} = 0.4,\ K_{ip} = 40$	
Voltage control	$K_{pv} = 0.25,\ K_{iv} = 25$	
PLL	$K_{p\mathrm{PLL}} = 60, K_{i\mathrm{PLL}} = 1400$	

TABLE II: Parameters of Model 2 and Type-4 wind testbed

Parameter	Value (SI)	Per-unit (pu)
# of WT	50	
Rated power	2 MW	0.9
DC-link voltage	1100 V	
Rated voltage	575 V	1
Nominal freq.	60 Hz	1
X_d, X_q	313 mΩ, 114 mΩ	1.305, 0.474
X'_d	71.0 mΩ	0.296
X''_d, X''_q	60.5 mΩ, 58.3 mΩ	0.252, 0.243
R_s,X_l	1.44 mΩ, 40.8 mΩ	0.006, 0.18
T'_{do}, T''_{do}	4.49 s, 0.0681 s	
T''_q	0.0513 s	
Inertial, poles	9.69 J, 2	
Friction factor	0.01	
L_{boost}	1.2 mH	
C_{dc}, τ	90 mF, 0.0272 s	
$L_1(X_1), R_1$	0.06 mH, 0.45 mΩ	0.15, 0.003
$C_1(B_1)$	3.6 mF	0.203
$L_{T1}(X_{T1}), R_{T1}$	0.15 mH, 5.65 mΩ	0.02, 0.002
$L_{T2}(X_{T2}), R_{T2}$	17.35 mH, 655 mΩ	0.03, 0.003
$L_2(X_2)$	$0.52 \rightarrow 1.21$ H	$0.45 \rightarrow 1.05$
R_2	$19.6 \rightarrow 45.8\ \Omega$	$0.045 \rightarrow 0.105$
Current control	$K_{pi} = 0.48,\ K_{ii} = 3.28$	
dc control	$K_{pp} = 0.4,\ K_{ip} = 40$	
Voltage control	$K_{pv} = 0.25,\ K_{iv} = 25$	
PLL	$K_{p\mathrm{PLL}} = 60\ K_{i\mathrm{PLL}} = 1400$	

REFERENCES

[1] N. P. W. Strachan and D. Jovcic, "Stability of a variable-speed permanent magnet wind generator with weak ac grids," *IEEE Transactions on Power Delivery*, vol. 25, no. 4, pp. 2779–2788, Oct 2010.

[2] J. Hu, Y. Huang, D. Wang, H. Yuan, and X. Yuan, "Modeling of grid-connected dfig-based wind turbines for dc-link voltage stability analysis," *IEEE Transactions on Sustainable Energy*, vol. 6, no. 4, pp. 1325–1336, Oct 2015.

[3] Y. Zhou, D. D. Nguyen, P. C. Kjr, and S. Saylors, "Connecting wind power plant with weak grid - challenges and solutions," in *2013 IEEE Power Energy Society General Meeting*, July 2013, pp. 1–7.

[4] S. H. Huang, J. Schmall, J. Conto, J. Adams, Y. Zhang, and C. Carter, "Voltage control challenges on weak grids with high penetration of wind generation: Ercot experience," in *2012 IEEE Power and Energy Society General Meeting*, July 2012, pp. 1–7.

[5] H. Liu, X. Xie, J. He, T. Xu, Z. Yu, C. Wang, and C. Zhang, "Subsynchronous interaction between direct-drive pmsg based wind farms and weak ac networks," *IEEE Transactions on Power Systems*, vol. 32, no. 6, pp. 4708–4720, 2017.

[6] L. Fan and Z. Miao, "An explanation of oscillations due to wind power plants weak grid interconnection," *IEEE trans. Sustainable Energy*, vol. 9, no. 1, pp. 488–490, Jan 2018.

[7] L. Fan, "Modeling type-4 wind in weak grids," *accepted, IEEE trans. Sustainable Energy*, Jun 2018.

[8] L. Fan and Z. Miao, "Wind in weak grids: 4 hz or 30 hz oscillations," *to appear, IEEE trans. Power Systems*.

[9] A. Dissanayaka, J. Wiebe, and A. Isaacs. (2018, March) Panhandle and South Texas Stability and System Strength Assessment. Electranix.

[10] B. Wu, Y. Lang, N. Zargari, and S. Kouro, *Power conversion and control of wind energy systems*. John Wiley & Sons, 2011, vol. 76.

[11] X. Yuan, F. Wang, D. Boroyevich, Y. Li, and R. Burgos, "Dc-link voltage control of a full power converter for wind generator operating in weak-grid systems," *IEEE Transactions on Power Electronics*, vol. 24, no. 9, pp. 2178–2192, Sept 2009.

[12] H. T. Ma, P. B. Brogan, K. H. Jensen, and R. J. Nelson, "Sub-synchronous control interaction studies between full-converter wind turbines and series-compensated ac transmission lines," in *2012 IEEE Power and Energy Society General Meeting*, July 2012, pp. 1–5.

[13] L. Zhang, L. Harnefors, and H. P. Nee, "Power-synchronization control of grid-connected voltage-source converters," *IEEE Transactions on Power Systems*, vol. 25, no. 2, pp. 809–820, May 2010.

[14] J. Alipoor, Y. Miura, and T. Ise, "Power system stabilization using virtual synchronous generator with alternating moment of inertia," *IEEE Journal of Emerging and Selected Topics in Power Electronics*, vol. 3, no. 2, pp. 451–458, 2015.

[15] K. Givaki, D. Chen, and L. Xu, "Current error based compensations for vsc current control in weak grid for wind farm applications," *IEEE Transactions on Sustainable Energy*, pp. 1–1, 2018.

[16] A. Egea-Alvarez, S. Fekriasl, F. Hassan, and O. Gomis-Bellmunt, "Advanced vector control for voltage source converters connected to weak grids," *IEEE Transactions on Power Systems*, vol. 30, no. 6, pp. 3072–3081, Nov 2015.

[17] K. Clark, N. W. Miller, and J. J. Sanchez-Gasca, "Modeling of GE wind turbine-generators for grid studies," GE Energy, Tech. Rep., April 2010.

[18] A. Yazdani and R. Iravani, *Voltage-sourced converters in power systems: modeling, control, and applications*. John Wiley & Sons, 2010.